A comprehensive investigation of multilayer $Ti_3C_2T_x$ MXene for supercapacitors in alkaline and acidic media

A.B. Tugelbayeva[1], B.K. Balgabayeva[1,2], F. Sultanov[1,3], Zh.A. Supiyeva[1,2]*

[1]Satbayev University, Almaty, Kazakhstan
[2]Al-Farabi Kazakh National University, Almaty, Kazakhstan
[3]National Laboratory Astana, Nazarbayev University, Astana, Kazakhstan
*E-mail: *zhazira.supiyeva@kaznu.kz*

Multilayer $Ti_3C_2T_x$ MXene was synthesized from Ti_3AlC_2 MAX phase via hydrofluoric acid etching followed by a gentle shaking-assisted delamination strategy, yielding well-preserved layered structures with expanded interlayer spacing of ~1.2-1.3 nm. Structural and spectroscopic analyses confirmed effective removal of Al layers and the formation of functionalized accordion-like MXene sheets. The electrochemical behavior was systematically investigated in symmetric two-electrode cells using alkaline and acidic electrolytes. The MXene electrode exhibited quasi-rectangular CV curves and symmetric charge–discharge profiles in alkaline media, indicating predominantly capacitive charge storage with good reversibility and rate capability. Significantly higher capacitance and improved retention were obtained in 6 M KOH, reaching ~70-72 $F\,g^{-1}$ at low scan rates, which is attributed to enhanced ionic conductivity, reduced charge-transfer resistance, and faster ion diffusion, as further supported by EIS analysis. In contrast, the acidic electrolyte showed distorted CV responses and increased polarization, suggesting slower charge-transfer kinetics and diffusion limitations. These findings highlight the decisive role of electrolyte chemistry in governing charge-storage mechanisms and demonstrate the strong potential of multilayer $Ti_3C_2T_x$ MXene for supercapacitor applications in concentrated alkaline electrolytes.

Keywords: MXene $Ti_3C_2T_x$; MAX phase Ti_3AlC_2; supercapacitor; aqueous electrolytes; electrochemical energy storage.

Сілтілі және қышқылды орталардағы суперконденсаторларға арналған көпқабатты $Ti_3C_2T_x$ MXene материалын кешенді зерттеу

А.Б. Тұгелбаева[1], Б.К. Балғабаева[1,2], Ф. Султанов[1,3], Ж.А. Супиева[1,2]*

[1] Қ.И. Сәтбаев атындағы Қазақ ұлттық зерттеу техникалық университеті, Алматы, Қазақстан
[2] Әл-Фараби атындағы Қазақ ұлттық университеті, Алматы, Қазақстан
[3]Астана ұлттық зертханасы, Назарбаев Университеті, Астана, Қазақстан
*E-mail: *zhazira.supiyeva@kaznu.kz*

Көпқабатты $Ti_3C_2T_x$ MXene Ti_3AlC_2 MAX-фазасынан фторсутек қышқылымен өңдеу және кейіннен жұмсақ шайқау арқылы қабаттарын ажырату әдісімен синтезделді. Нәтижесінде қабатаралық арақашықтығы шамамен 1,2-1,3 нм болатын жақсы сақталған қабатты құрылым алынды. Құрылымдық және спектроскопиялық талдаулар алюминий қабаттарының тиімді жойылғанын және аккордеон тәрізді морфологиясы бар функционалданған MXene қабаттарының түзілгенін растады. Электрохимиялық қасиеттері сілтілі және қышқылды электролиттерді пайдалана отырып, симметриялы екі электродты ұяшықтарда жүйелі түрде зерттелді. MXene негізіндегі электрод сілтілі ортада циклдік вольтамперограммалардың квазитікбұрышты пішінін және симметриялы заряд–разряд қисықтарын көрсетті, бұл зарядтың негізінен сыйымдылық механизмі арқылы жинақталатынын, процестің жақсы қайтымдылығын және жоғары жылдамдықтық сипаттамаларын дәлелдейді. Ең жоғары меншікті сыйымдылық пен тұрақтылық 6 М КОН ерітіндісінде байқалып, төмен сканерлеу жылдамдықтарында шамамен 70-72 Ф/г мәніне жетті. Бұл жоғары иондық өткізгіштікке, заряд тасымалдау кедергісінің төмендеуіне және иондардың жылдам диффузиясына байланысты болып, электрохимиялық импеданстық спектроскопия (EIS) нәтижелерімен де расталды. Ал қышқылды электролитте циклдік вольтамперограммалардың бұрмалануы және поляризацияның артуы байқалды, бұл заряд тасымалдау кинетикасының баяулауын және диффузиялық шектеулердің бар екенін көрсетті. Алынған нәтижелер заряд жинақтау механизмдерін анықтауда электролиттің химиялық табиғатының шешуші рөл атқаратынын көрсетеді және көпқабатты $Ti_3C_2T_x$ MXene материалының концентрлі сілтілі электролиттердегі суперконденсаторлар үшін жоғары әлеуетке ие екенін дәлелдейді.

Түйін сөздер: $Ti_3C_2T_x$ MXene; Ti_3AlC_2 MAX-фаза; суперконденсатор; сулы электролиттер; энергияны электрохимиялық жинақтау.

Комплексное исследование многослойного MXene $Ti_3C_2T_x$ для суперконденсаторов в щелочных и кислых средах

А.Б. Тугелбаева[1], Б.К. Балгабаева[1,2], Ф. Султанов[1,3], Ж.А. Супиева[1,2]*

[1]Казахский национальный исследовательский технический университет имени К.И. Сатпаева, Алматы, Казахстан
[2] Казахский национальный университет имени аль-Фараби, Алматы, Казахстан
[3]Национальная лаборатория Астана, Назарбаев Университет, Астана, Казахстан
*E-mail: *zhazira.supiyeva@kaznu.kz*

Многослойный MXene $Ti_3C_2T_x$ был синтезирован из MAX-фазы Ti_3AlC_2 методом травления HF с последующим мягким расслоением при встряхивании, что обеспечило получение хорошо сохранившихся слоистых структур с увеличенным межслоевым расстоянием около 1,2-1,3 нм. Структурный и спектроскопический анализ подтвердил эффективное удаление слоев Al и формирование функционализированных MXene слоев характерной аккордеоноподобной морфологией. Электрохимические свойства были систематически исследованы в симметричных двухэлектродных ячейках с использованием щелочных и кислых электролитов. Электрод на основе MXene продемонстрировал квази-прямоугольные кривые циклической вольтамперометрии и симметричные кривые заряд–разряд в щелочной среде, что свидетельствует о преимущественно емкостном механизме накопления заряда, хорошей обратимости и высокой скоростной способности. Наиболее высокие значения удельной емкости и стабильности были получены в 6 М КОН, достигая около 70-72 Ф/г при низких скоростях сканирования, что обусловлено повышенной ионной проводимостью, снижением сопротивления переносу заряда и ускоренной диффузией ионов, что также подтверждается результатами электрохимической импедансной спектроскопии (EIS). Напротив, в кислой среде наблюдались искаженные кривые циклической вольтамперометрии и повышенная поляризация, указывающие на замедленную кинетику переноса заряда и ограничения диффузии. Полученные результаты подчеркивают решающую роль химической природы электролита в формировании механизмов накопления заряда и демонстрируют высокий потенциал многослойного MXene $Ti_3C_2T_x$ для применения в суперконденсаторах с концентрированными щелочными электролитами.

Ключевые слова: MXene $Ti_3C_2T_x$; MAX-фаза Ti_3AlC_2; суперконденсатор; водные электролиты; электрохимическое накопление энергии.

(2026) Chem Bull Kaz Nat Univ 2:12-24

CHEMICAL BULLETIN
of Kazakh National University
http://bulletin.chemistry.kz/

IRSTI 44.29.29 https://doi.org/10.15328/cb2026_127

Article

A comprehensive investigation of multilayer $Ti_3C_2T_x$ MXene for supercapacitors in alkaline and acidic media

A.B. Tugelbayeva[1], B.K. Balgabayeva[1,2], F. Sultanov[1,3], Zh.A. Supiyeva[1,2]*

[1]Satbayev University, Satpaev str. 22a, 050013 Almaty, Kazakhstan
[2]Al-Farabi Kazakh National University, al-Farabi ave. 71, 050040 Almaty, Kazakhstan
[3]National Laboratory Astana, Nazarbayev University, Kabanbay Batyr ave. 53, 010000 Astana, Kazakhstan
*E-mail: *zhazira.supiyeva@kaznu.kz*

1. Introduction

The global transition toward clean and renewable energy sources demands the development of safe and reliable energy storage technologies, particularly for portable electronics [1,2]. Electrochemical capacitors store energy through reversible ion adsorption at electrode surfaces, offering high power density but limited energy density. Recent strategies to enhance their energy output involve introducing faradaic contributions via pseudocapacitive materials and surface functionalization. In this context, introducing additional faradaic charge-storage mechanisms has been recognized as an effective strategy to enhance the energy density of electrochemical capacitors[1,3].

A breakthrough in two-dimensional materials was achieved in 2011, when selective chemical etching of the Al layer from Ti_3AlC_2 MAX phase using hydrofluoric acid enabled the synthesis of MXenes, a class of transition metal carbides and nitrides with layered morphology [4]. Their unique combination of metallic conductivity, hydrophilicity, and rich surface chemistry has positioned MXenes as a highly promising class of materials for electrochemical energy storage applications [5-7]. The parent MAX phases, generally described by the formula $M_{n+1}AX_n$, are layered hexagonal carbides and nitrides in which early transition metal-carbon/nitrogen slabs (M–X) are separated by an A-element layer, typically Al. Strong covalent and metallic M–X bonding provides structural stability, whereas weaker metallic M–A bonding enables selective removal of the A-layer, forming MXenes [8,9]. In the case of Ti_3AlC_2 HF selectively cleaves Ti–Al bonds, dissolving aluminum as soluble AlF_3 species while preserving the Ti-C framework [10-12]. The resulting $Ti_3C_2T_x$ nanosheets are terminated with surface functional groups such as –O, –OH, and –F, which enhance hydrophilicity, colloidal stability, and compatibility with aqueous processing [10,13,14].

Since the original HF-based synthesis, several alternative etching strategies have been developed. One of the most widely used approaches involves in situ HF generation through the reaction of LiF with HCl, which enables gradual fluoride release and simultaneous Li^+ intercalation, promoting structural swelling and partial delamination during etching, often assisted by ultrasonication [15]. Although this method is considered safer and can yield MXenes with enlarged interlayer spacing, it often results in incomplete etching, residual aluminum impurities, or less controlled surface terminations. In addition, the use of ultrasonication may induce significant structural degradation, leading to a drastic reduction in the lateral size of MXene flakes-from approximately 4.4 µm to 1.0 µm within 15 min, and further down to 350 nm or even 130 nm upon prolonged treatment [16,17]. This process causes severe fragmentation of the layered structure and generates a high density of edge defects, which can adversely affect the electrical conductivity and electrochemical stability of the material.

Other emerging methods, including molten-salt and electrochemical etching, eliminate the use of HF but typically require high temperatures or complex instrumentation and may alter the stoichiometry of the resulting MXene. Despite these developments, direct HF etching remains the most reliable and reproducible approach for producing high-purity $Ti_3C_2T_x$ with well-defined layered morphology, minimal residual aluminum content, and high electronic conductivity. Accordingly, HF etching was selected as the primary synthesis route in this work to obtain structurally uniform and conductive MXene suitable for subsequent modification.

Received 09 Mar 2026; Received in revised form 22 Apr 2026; Accepted 28 Apr 2026; Available online 30 Jun 2026.

Building on the high-quality $Ti_3C_2T_x$ MXene obtained via HF etching, this study further explores the development of $Ti_3C_2T_x$ based composites [18].

In this work, a controlled synthesis of $Ti_3C_2T_x$ MXene is achieved using a gentle shaking-assisted delamination approach, which preserves the structural integrity of the material without the use of ultrasonication. The electrochemical behavior of $Ti_3C_2T_x$ was systematically investigated in different aqueous electrolytes (1 M H_2SO_4, 1 M KOH, and 6 M KOH) using cyclic voltammetry (CV), galvanostatic charge–discharge (GCD), and electrochemical impedance spectroscopy (EIS). It is demonstrated that the electrochemical performance strongly depends on both the type and concentration of the electrolyte, with the highest specific capacitance obtained in concentrated alkaline medium.

2. Experiment

2.1 Materials

Titanium aluminum carbide (Ti_3AlC_2, Carbon Ukraine) MAX phase was used as the precursor for MXene synthesis. Hydrofluoric acid (HF, 48 wt%, Honeywell Fluka) was used as the etching agent. *N*-methyl-2-pyrrolidone (NMP, ≥99.0%) and poly(vinylidene fluoride) (PVDF, $M_n \approx$ 534,000 g mol^{-1}, Sigma-Aldrich) were used as received. Super P conductive carbon black was used as the conductive additive. Potassium hydroxide (KOH) and sulfuric acid (H_2SO_4) were used as electrolytes. All chemicals utilized in this work were of analytical purity and applied without any additional treatment.

2.2 Preparation of $Ti_3C_2T_x$ MXene powder

$Ti_3C_2T_x$ MXene was synthesized by selectively etching aluminum layers from Ti_3AlC_2 MAX phase powder using hydrofluoric acid. Briefly, 1 g of Ti_3AlC_2 powder was gradually added to 20 mL of concentrated HF (48 wt%) in a high-density polyethylene (HDPE) container equipped with a magnetic stir bar [11]. The mixture was continuously stirred at room temperature (~25°C) for 8 h under a fume hood. No additional intercalating agents were used during the etching process.

The formation mechanism of $Ti_3C_2T_x$ MXene is illustrated in Figure 1, while the corresponding reactions are described by the following equations.

During the etching process, aluminum atoms were selectively removed according to the following reaction:

$$Ti_3AlC_2 + 3HF \rightarrow Ti_3C_2T_x + AlF_3 + 1/2H_2\uparrow$$

$$Ti_3C_2 + 2HF \rightarrow Ti_3C_2F_2 + H_2$$

$$Ti_3C_2 + 2H_2O \rightarrow Ti_3C_2(OH)_2 + H_2$$

where $T_x = -O, -OH, -F$ denotes the surface terminations formed during etching [19]. The color of the suspension gradually changed from gray to dark black, confirming the transformation of MAX phase into $Ti_3C_2T_x$ MXene.

Following the etching process (Figure 2), the resulting suspension was washed multiple times with deionized water and subjected to centrifugation at 5000 rpm for 5 min in each cycle until the supernatant reached a near-neutral pH (~6-7), indicating effective removal of residual HF and AlF_3 species. Typically, 6-7 washing cycles were required using ~50 mL of DI water per cycle. Prior to each centrifugation step, the suspension was subjected to mechanical shaking at 250 rpm for 5 min to promote delamination of the etched $Ti_3C_2T_x$ layers. Ultrasonic treatment was intentionally avoided to prevent structural fragmentation and edge defects. The resulting sediment was vacuum-filtered through a PVDF membrane filter (0.22 µm pore size, 47 mm diameter) to obtain a uniform black $Ti_3C_2T_x$ film. The film was rinsed with DI water and dried under vacuum at 60°C for 8 h. Subsequently, the dried MXene $Ti_3C_2T_x$ film was gently peeled off and ground in an agate mortar to obtain a fine powder. The final yield of $Ti_3C_2T_x$ was approximately 0.99 g per 1 g of Ti_3AlC_2, corresponding to a yield of ~99%.

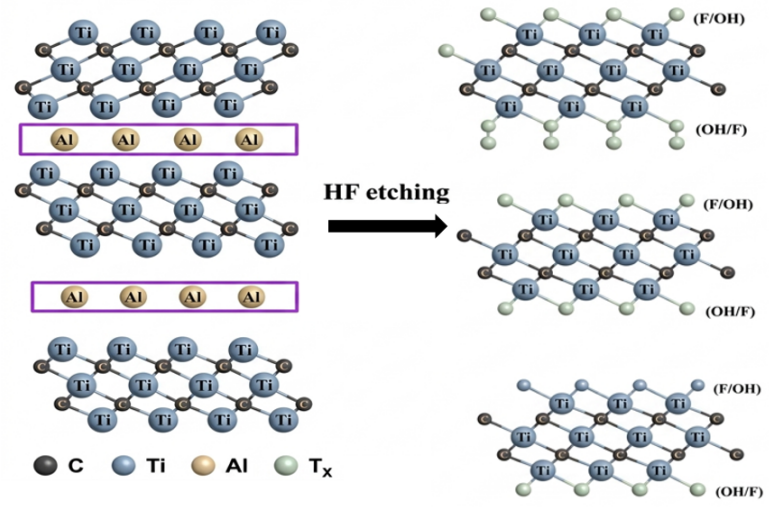

Figure 1 – Schematic illustration of the synthesis of MXene $Ti_3C_2T_x$ from the MAX phase Ti_3AlC_2

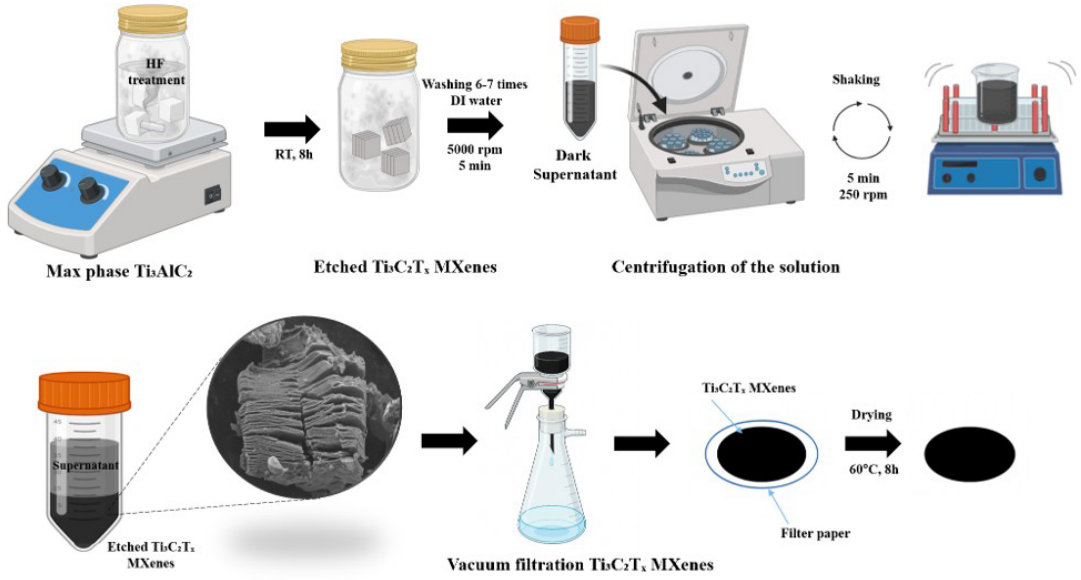

Figure 2 – Methodology scheme of synthesis $Ti_3C_2T_x$ Mxene powder

2.3 Characterization

Phase composition and crystallinity of the synthesized materials were analyzed using X-ray diffraction (XRD) on a Rigaku MiniFlex BENCHTOP diffractometer, operating in the 2θ range of 10-60° with a step size of 0.01°. The microstructure and surface morphology of the MXene powder were examined using a JEOL JSM-IT890 scanning electron microscope (SEM, Japan). Chemical states and elemental composition were analyzed by X-ray photoelectron spectroscopy (XPS, Thermo Scientific NEXSA). In addition, transmission electron microscopy (TEM, JEOL), Raman spectroscopy (LabRAM, Horiba), thermogravimetric analysis (TGA, STA6000, Perkin Elmer) were employed in the scan rate 10°C and X-ray photoelectron spectroscopy (XPS, NEXSA, Thermo Scientific) with a monochromated low-power Al Ka X-ray source - 1486.6 eV.

2.4 Electrode preparation

For electrode fabrication, $Ti_3C_2T_x$ MXene powder, Super P conductive carbon black, and PVDF binder were mixed in a mass ratio of 8:1:1 using NMP as the solvent. The components were thoroughly ground in an agate mortar to obtain a homogeneous slurry. The slurry was cast onto graphite foil using the doctor blade technique with a controlled thickness of approximately 22 µm and dried under vacuum at 60°C for 12 h. The obtained electrode was defined as the active material for electrochemical measurements. Circular electrodes with a diameter of 10 mm and an active material mass loading of approximately 6-7 mg were cut using laser cutting equipment to ensure uniform geometry. A symmetric supercapacitor cell was assembled in a two-electrode Swagelok-type configuration using a glass fiber separator (Whatman GF/A) soaked in 1 M KOH, 6 M KOH and 1 M H_2SO_4 aqueous electrolytes.

2.5 Electrochemical testing

Electrochemical measurements were conducted using a potentiostat/galvanostat (SP150E, BioLogic) in a two-electrode Swagelok-type cell configuration. Cyclic voltammetry (CV) was performed within a potential window of 0-1 V at scan rates ranging from 2 to 100 mV s^{-1}. Galvanostatic charge–discharge (GCD) tests were carried out at current densities between 0.2 and 2 A g^{-1}. Electrochemical impedance spectroscopy (EIS) measurements were performed over the same voltage window in the frequency range of 1 MHz to 10 mHz.

The specific capacitance was calculated from the GCD curves using the following equation:

and from CV curves using:

here I is the discharge current, Δt is the discharge time (s), ΔV is the potential window excluding IR drop (V), m is the mass

$$C_{GCD} = \frac{4 * I * \Delta t}{\Delta V * m}$$

of active material (g), A is the integrated area of the CV curve, v

$$C_{CV} = \frac{2 * A}{m_{total} * v * \Delta V}$$

is the scan rate (V s^{-1}), and m_{totaal} is the total mass of active material in both electrodes (g).

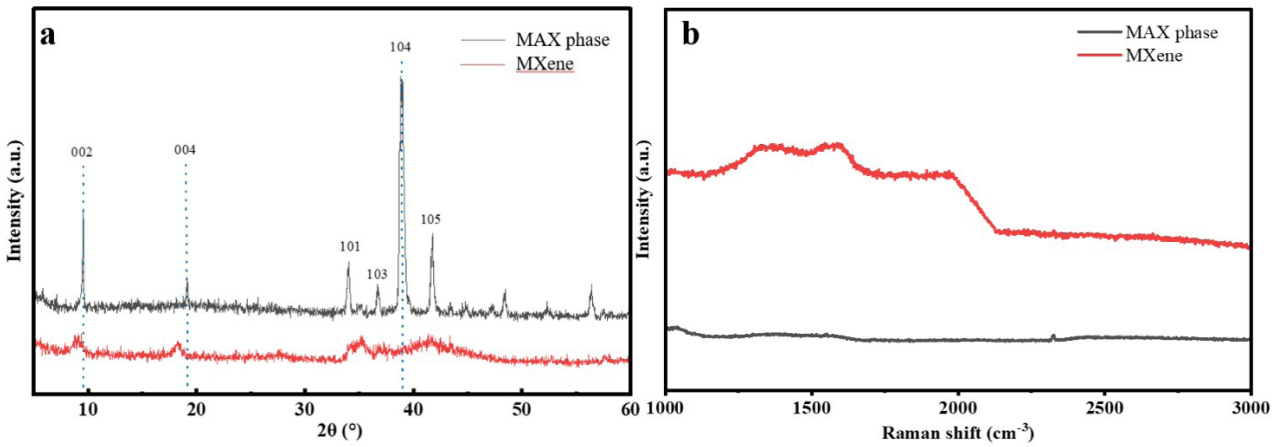

Figure 3 – XRD analysis (a) and Raman shift (b) of $Ti_3C_2T_x$ Mxene

3. Results and Discussion

3.1 Structural analysis

The structural evolution from Ti_3AlC_2 MAX phase to $Ti_3C_2T_x$ MXene was investigated by X-ray diffraction (XRD), as presented in Figure 3. The pristine Ti_3AlC_2 exhibits sharp and well-defined diffraction peaks corresponding to the (002), (004), (101), (103), (104), and (105) crystallographic planes, confirming the highly ordered hexagonal structure of the MAX precursor. Following selective etching of the Al layers, a pronounced modification of the diffraction pattern is observed, indicating the successful formation of $Ti_3C_2T_x$ MXene.

In particular, the characteristic (002) peak of Ti_3AlC_2 shifts toward lower diffraction angles and becomes noticeably broadened after etching, suggesting a significant increase in the interlayer spacing. This shift is attributed to the removal of Al atomic layers and the introduction of surface termination groups (–O, –OH, and –F), as well as the intercalation of water molecules between adjacent MXene sheets. Concurrently, the substantial suppression or disappearance of non-basal reflections, especially the (104) peak located near 39°, further confirms the effective elimination of Al and the disruption of the long-range crystallographic ordering of the MAX phase.

These observations collectively demonstrate the successful transformation of Ti_3AlC_2 into few-layered $Ti_3C_2T_x$ MXene with expanded interlayer spacing, reduced crystallinity, and a characteristic lamellar structure formed during the etching and delamination processes.

The interlayer spacing of $Ti_3C_2T_x$ was further estimated from the position of the (002) reflection using Bragg's law [20,21]. The diffraction patterns were recorded using Cu Kα radiation (λ = 1.5406 Å). The low-angle position of the (002) peak indicates a markedly enlarged interlayer distance compared with the parent MAX phase, confirming effective exfoliation and interlayer expansion of the MXene structure. The calculated d-spacing was approximately 11.9 Å (1.19 nm), consistent with previously reported values for multilayer $Ti_3C_2T_x$ MXene [22].

The Raman spectra of the Ti_3AlC_2 MAX phase and the corresponding MXene, presented in Figure 3b, demonstrate significant structural and bonding changes induced by the selective etching process. The Ti_3AlC_2 MAX phase exhibits relatively weak but well-defined Raman features, reflecting its highly ordered crystalline structure. In contrast, the MXene sample shows several pronounced and broadened features across the range of 500-2000 cm^{-1}, indicating the transformation into surface-terminated $Ti_3C_2T_x$ layers. Notably, the broad bands in the 1369-1589 cm^{-1} region can be attributed to the D and G bands of disordered carbon, typically associated with defects and carbonaceous species, which may arise from structural disorder, partial oxidation, or processing induced effects [23,24], while the band at ~625 cm^{-1} further indicates surface termination evolution and oxidation-related structural modifications of $Ti_3C_2T_x$.

XPS analysis was conducted to characterize the surface chemistry and elemental distribution of the obtained $Ti_3C_2T_x$ MXene. The survey spectrum confirms the presence of Ti, C, O, and F elements and the absence of Al, indicating the successful removal of the A-layer and the formation of MXene with typical surface termination groups. High-resolution spectra reveal pronounced surface functionalization. The Ti 2p spectrum is dominated by oxidized titanium species, with the $2p_{3/2}$ peak at ~458.2 eV assigned to Ti^{4+} (Ti-O) and additional components at ~459.8 eV and ~456.8-457.2 eV corresponding to hydroxylated Ti and Ti^{3+} suboxide states, suggesting strong surface oxidation of the MXene flakes [25,26]. Consistently, the O 1s spectrum shows contributions at ~531.8 eV attributed to Ti-OH and at ~533–535 eV related to Ti-O and adsorbed oxygen species[27]. The C 1s spectrum is mainly characterized by a peak at ~284.8 eV corresponding to C-C bonds with partially overlapping Ti-C contributions, while additional components at ~286.5 eV and

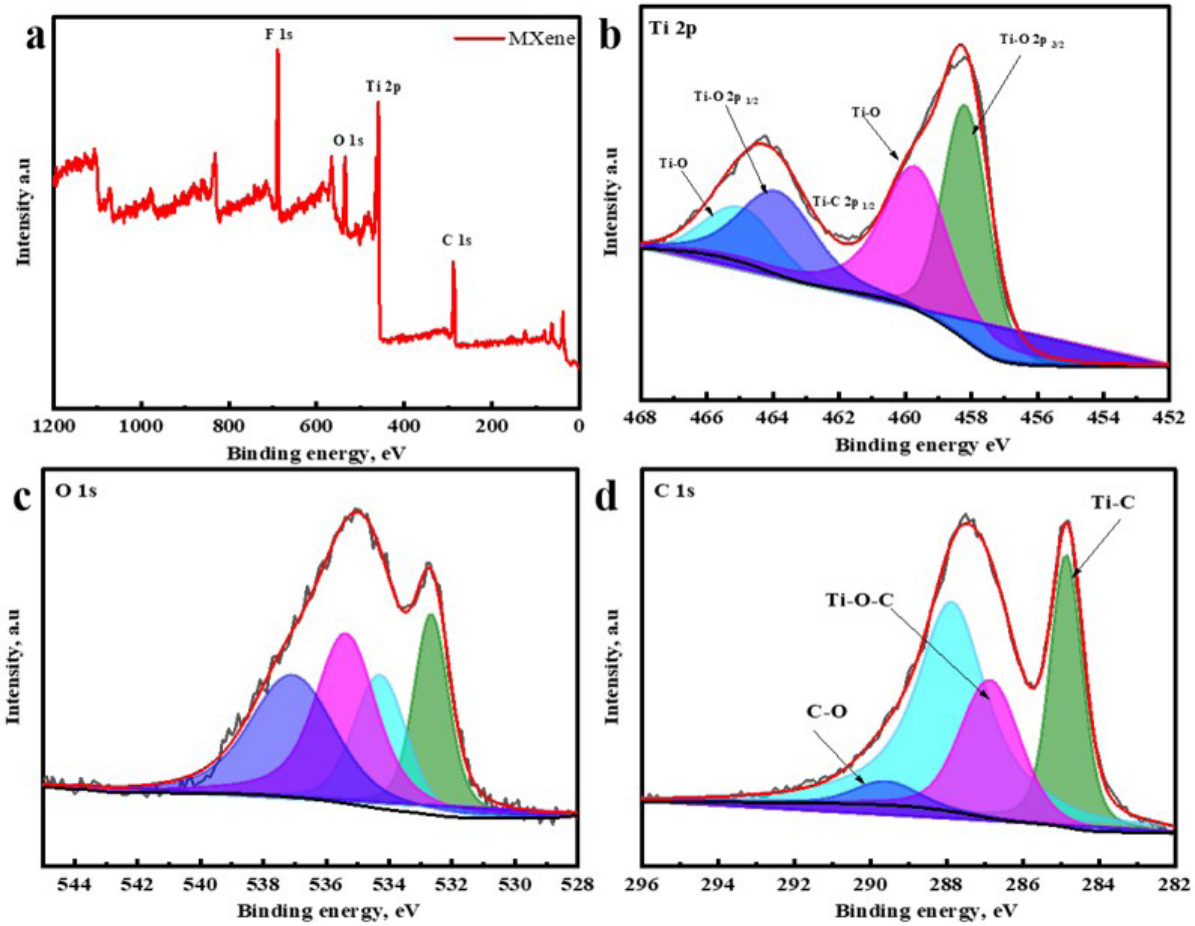

Figure 4 – XPS survey spectrum of $Ti_3C_2T_x$ MXene (a), high-resolution spectra of (b) Ti 2p, C 1s (c), O 1s (d)

~288.3 eV are assigned to C-O and O–C=O groups, confirming surface oxidation and interaction with termination species [28]. Overall, the results indicate a preserved MXene framework with significant surface termination and partial oxidation of Ti atoms.

3.2 Morphological and surface characterization

The enlarged interlayer spacing compared with the parent MAX phase confirms the successful removal of the A-layer and the formation of a delaminated MXene $Ti_3C_2T_x$ structure. Such gallery expansion is commonly attributed to the presence of surface terminations (–O, –OH, –F) and intercalated species, which improve electrolyte accessibility and facilitate ion transport. Moreover, the d-spacing values obtained from XRD are in good agreement with the interlayer distances estimated from HRTEM/IFFT analysis, indicating strong structural consistency across different characterization techniques.

The morphological evolution from Ti_3AlC_2 MAX phase to $Ti_3C_2T_x$ MXene was investigated using scanning electron microscopy (SEM), as shown in Figure 5. The pristine Ti_3AlC_2 (Figure 5a,b) exhibits a dense and compact morphology composed of closely stacked, irregularly shaped particles. The layered architecture of the MAX phase is clearly visible, with well-defined edges and relatively smooth surfaces, reflecting the strong bonding between Ti–Al–C atomic layers. The interlayer spacing of the MXene precursor was estimated to be in the range of 68-118 nm.

After selective etching of Al layers, $Ti_3C_2T_x$ MXene (Figure 5c,d) exhibits a pronounced morphological transformation into an open, accordion-like structure with clearly separated lamellae. The expanded layered morphology provides increased surface area and shortened ion diffusion pathways, which are beneficial for electrochemical performance.

The compositional and morphological features were further examined using SEM coupled with energy-dispersive X-ray spectroscopy (SEM–EDS), as presented in Figure 6. The MAX phase (Figure 6a) retains a compact and densely packed layered structure, characteristic of well-crystallized Ti_3AlC_2. The smooth particle surfaces and limited interlayer spacing indicate strong metallic bonding involving Al layers. In contrast, the etched MXene (Figure 6b) displays an open and delaminated morphology with separated nanosheets, consistent with the structural evolution observed in SEM and the XRD peak shift of the (002) reflection toward lower 2θ values.

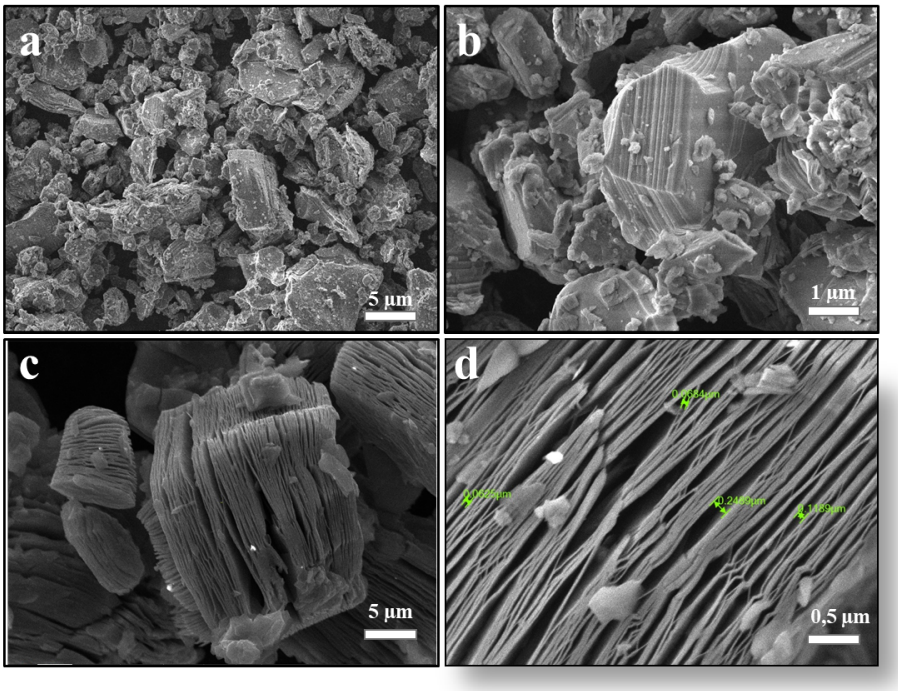

Figure 5 – SEM analysis of Max phase (a,b) and $Ti_3C_2T_x$ Mxene powder (c,d)

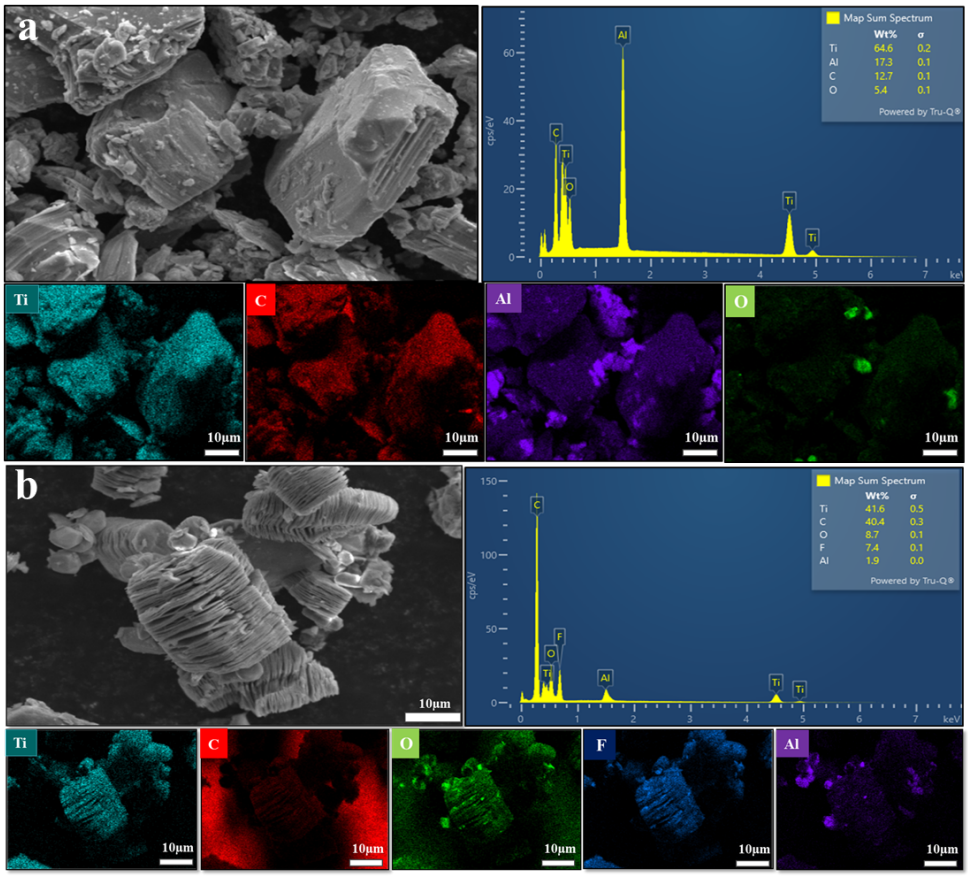

Figure 6 – SEM–EDS analysis of the MAX phase (a) and $Ti_3C_2T_x$ MXene powder (b)

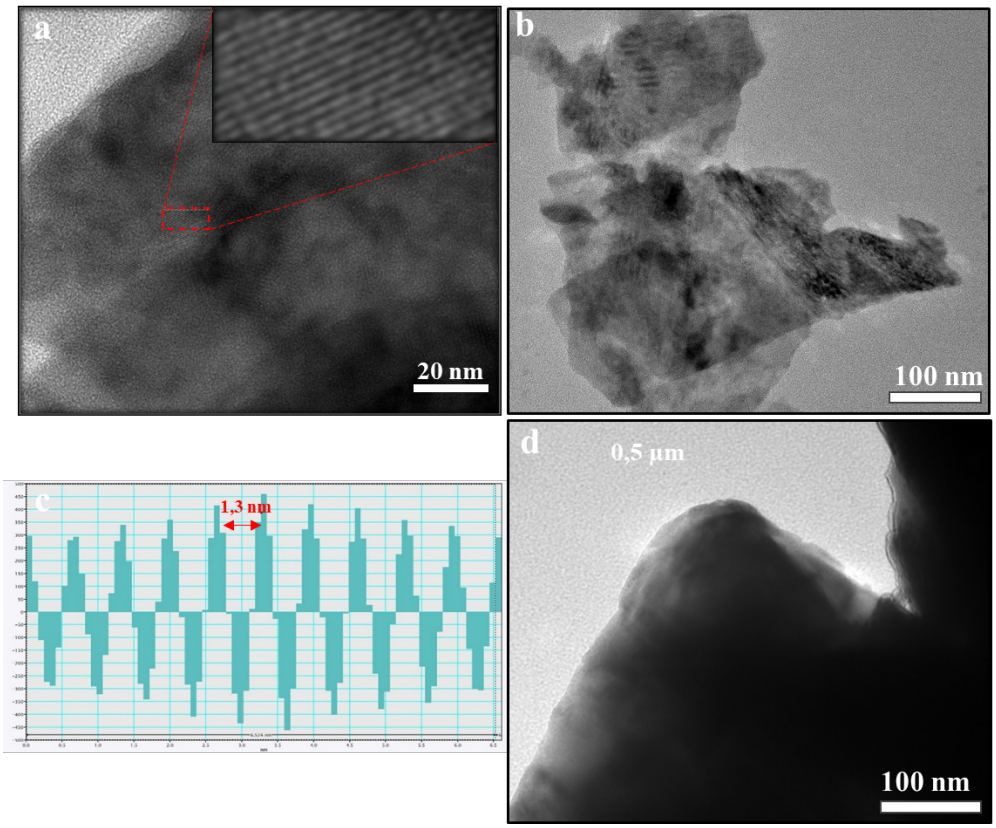

Figure 7 – TEM images of $Ti_3C_2T_x$ MXene IFFT patterns (a-c) and the parent MAX phase (d)

The EDS spectra further confirm the compositional transformation from Ti_3AlC_2 to $Ti_3C_2T_x$ MXene. The pristine MAX phase (Figure 6a) shows a pronounced Al signal corresponding to the Ti_3AlC_2 stoichiometry. After etching, the MXene sample (Figure 7b) exhibits a significant reduction in Al content (~1.9 wt%), indicating efficient removal of the Al layers. The residual trace amount of Al is likely associated with incomplete etching within multilayer particles, which is commonly reported for MXene synthesis. Additionally, the increased oxygen content supports the formation of surface functional groups (–O, –OH, –F) generated during the etching and delamination processes. Overall, these results verify the successful conversion of Ti_3AlC_2 into few-layered $Ti_3C_2T_x$ MXene with expanded interlayer spacing and functionalized surfaces.

High-resolution TEM analysis was performed to further elucidate the microstructure of $Ti_3C_2T_x$ MXene. As shown in Figure7 (a-c), well-defined layered lattice fringes are observed within the $Ti_3C_2T_x$ flakes, confirming the formation of an ordered lamellar structure after selective etching of the MAX phase [29]. The interlayer spacing, determined from the IFFT line profile by measuring the distance between adjacent intensity maxima, is approximately 1.3 nm [6,30]. This enlarged interlayer distance indicates effective removal of the Al layers and the presence of surface functional groups, leading to expanded MXene galleries. Such structural expansion is known to enhance electrolyte accessibility and facilitate ion transport within the layered framework [31]. For comparison, the TEM image of the parent MAX phase shown in Figure8d exhibits a more compact layered structure, further confirming the successful transformation from Ti_3AlC_2 to $Ti_3C_2T_x$ MXene [32].

3.3 Thermal analysis (TGA)

The thermogravimetric analysis (TGA) was conducted to compare the thermal behavior of the MAX phase and the corresponding $Ti_3C_2T_x$ MXene (Figure 8). The MAX phase exhibited negligible mass variation up to ~350°C, confirming its high thermal stability, followed by a gradual weight increase at elevated temperatures due to oxidation and formation of oxide phases.

In contrast, the MXene sample showed a multistep weight loss behavior. The initial mass decrease below ~150°C is attributed to the removal of adsorbed and interlayer water, reflecting the hydrophilic nature of surface terminations. A pronounced weight loss between 150 and 250°C corresponds to the elimination of intercalated species and surface functional groups (–OH, –F), confirming successful etching and delamination of the MAX precursor [33,34]. Further gradual mass change up to ~450°C is associated with progressive dehydroxylation and structural modification of $Ti_3C_2T_x$ layers. At higher temperatures, a slight mass increase is observed due to oxidation of MXene and formation of TiO_2.

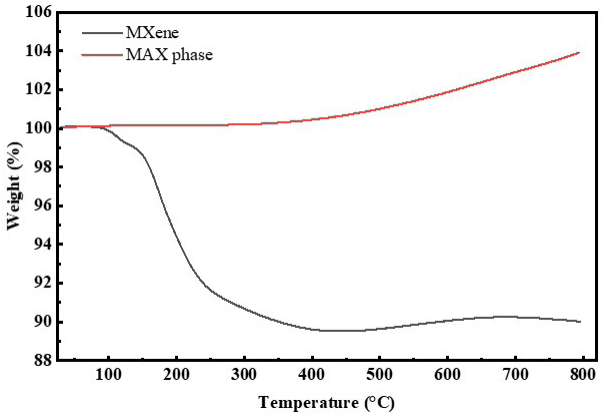

Figure 8 – TGA analysis of $Ti_3C_2T_x$ Mxene and Ti_3AlC_2 MAX phase powder

3.2 Electrochemical characterization

Figure 9 illustrates the electrochemical performance of the assembled $Ti_3C_2T_x$ MXene-based two-electrode Swagelok cell evaluated in 1 M KOH electrolyte. The cyclic voltammetry (CV) curves recorded at scan rates ranging from 2 to 100 mV s^{-1} within voltage windows of 0.6, 0.8, and 1.0 V (Figure 9a-d) exhibit quasi-rectangular shapes, indicating predominantly capacitive charge-storage behavior [35]. As the scan rate increases, the current response rises proportionally while the CV shape remains well preserved, demonstrating fast charge propagation and favorable rate capability.

The specific capacitance derived from CV measurements decreases with increasing scan rate, which is typical for capacitive materials due to diffusion limitations at higher rates. In 1 M KOH, the capacitance values are 50.3, 44.4, 40.7, and 36.9 Fg^{-1} at scan rates of 2, 20, 50, and 100 mV s^{-1}, respectively (Figure 9a-d). Notably, higher capacitance values of 69.2, 71.9, 68.9, and 65.3 F g^{-1} are obtained in 6 M KOH, indicating enhanced electrolyte conductivity and improved ion transport under concentrated alkaline conditions. At lower scan rates, electrolyte ions effectively penetrate the layered MXene galleries, enabling access to a larger electrochemically active surface area, whereas at higher scan rates partial diffusion limitation reduces the utilization of active sites.

The galvanostatic charge–discharge (GCD) profiles recorded at current densities from 0.2 to 2 A g^{-1} (Figure 9e-h) display nearly symmetric triangular shapes, confirming good electrochemical reversibility and high coulombic efficiency [36]. The linear voltage–time characteristics further indicate stable capacitive behavior. A relatively small IR drop observed at the beginning of discharge suggests low internal resistance, which can be attributed to the intrinsic electrical conductivity of $Ti_3C_2T_x$ and efficient electrolyte accessibility within the expanded layered structure.

Figure 10 presents the electrochemical response of the $Ti_3C_2T_x$ -based two-electrode cell in 6 M KOH electrolyte. The CV curves (Figure 10a-d) retain quasi-rectangular shapes over the entire scan-rate range, demonstrating improved rate performance compared with 6 M KOH. The enhanced current response reflects accelerated ion transport and reduced polarization effects in the concentrated electrolyte.

The GCD-derived capacitance values further confirm the superior performance in 6 M KOH. At all investigated current densities and voltage windows, the electrode delivers higher capacitance than in 1 M KOH. For instance, at 0.5 A g^{-1} and 1.0 V, the capacitance reaches 52.4 F g^{-1} in 6 M KOH compared with 44 F g^{-1} in 1 M KOH. Although capacitance decreases with increasing current density in both electrolytes, the retention is notably higher in 6 M KOH, indicating improved ionic conductivity and faster charge-transfer kinetics.

The galvanostatic charge–discharge profiles measured at current densities from 0.2 to 2 A g^{-1} (Figure 10 e-h) display nearly symmetric triangular shapes across all voltage windows, confirming good reversibility and stable capacitive behavior [37].

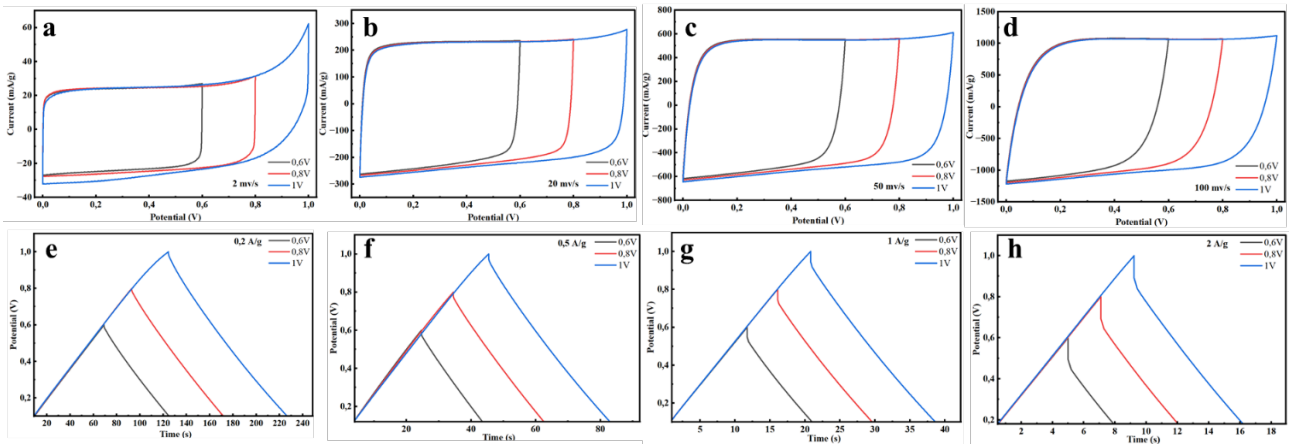

Figure 9 – Electrochemical behavior of the active material two-electrode Swagelok cell in 1 M KOH: CV curves at 2-100 mV s^{-1} within 0.6-1.0 V (a–d) and GCD profiles at 0.2-2 A g^{-1} recorded in identical voltage windows (e,h)

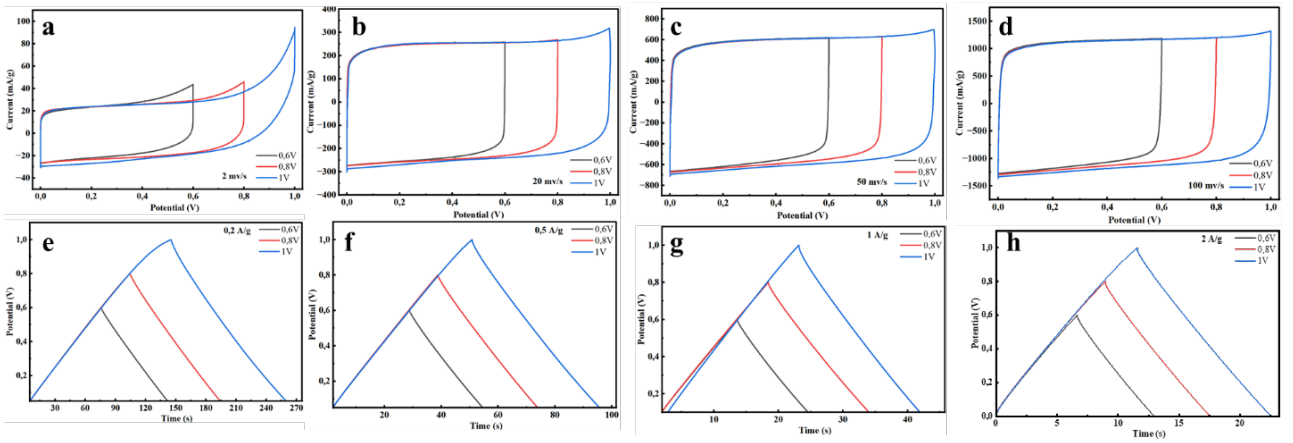

Figure 10 – Electrochemical behavior of the active material two-electrode Swagelok cell in 6 M KOH: CV curves at 2-100 mV s^{-1} within 0.6-1.0 V (a-d) and GCD profiles at 0.2-2 A g^{-1} recorded in identical voltage windows (e,f)

These results demonstrate that the $Ti_3C_2T_x$ based cell maintains efficient charge–discharge characteristics in 6 M KOH over a wide range of scan rates.

A comparison of the electrochemical performance of MXene-based supercapacitors reported in the literature is presented in Table 1. As shown in Table 1, the capacitance of $Ti_3C_2T_x$ strongly depends on the electrolyte type. In acidic electrolytes, symmetric configurations typically exhibit moderate capacitance values in the range of 45-64 F g^{-1}, which is associated with proton intercalation and increased polarization effects. In contrast, alkaline electrolytes (1 M and 6 M KOH) demonstrate higher capacitance values, reaching up to ~100 F g^{-1}, due to improved ion transport and more stable charge storage behavior. The results obtained in this work (~70-72 F g^{-1} in 6 M KOH) are consistent with previously reported data, confirming that concentrated alkaline electrolytes provide more favorable conditions for $Ti_3C_2T_x$ MXene electrodes.

The electrochemical behavior in acidic electrolyte was further evaluated using 1 M H_2SO_4, as shown in Figure 11-f. In contrast, to alkaline media, the CV curves exhibit pronounced deviations from ideal rectangular shapes, suggesting a significant contribution from faradaic reactions [39]. At low scan rates, the current response increases strongly with applied potential, indicating enhanced redox activity of surface functional groups.

With increasing scan rate, the distortion of the CV profiles for $Ti_3C_2T_x$ in 1 M H_2SO_4 becomes more pronounced, reflecting increased polarization and slower charge-transfer kinetics compared to alkaline media. The limited preservation of the CV shape at higher scan rates indicates a restricted rate capability, which is a consequence of the charge disproportion inherent in symmetric MXene-based cells in acidic electrolytes. While the negative electrode effectively stores charge via hydrogen electrosorption and hydronium ion intercalation, the positive electrode operates in a considerably narrower potential range, limited by poor anion intercalation and susceptibility to oxidative degradation [41]. Crucially, in a symmetric two-electrode cell with 1 M H_2SO_4 electrolyte, a stable electrochemical process is virtually impossible at voltages exceeding 0.6 V [35]. These features suggest that the charge-storage process in 1 M H_2SO_4 is less stable and more dominated by Faradaic reactions at the negative side, which restricts the practical operating voltage window and long-term stability of the symmetric device. In contrast, alkaline electrolytes provide better charge compensation and faster ion diffusion, resulting in the superior capacitive response observed in this study [1].

Table 1 – Overview of the electrochemical performance of MXene-based supercapacitors

№	Type of electrode	Confugration	Type of electrolytes	ΔV, V	C_{GCD} (F g^{-1})	Scan rate, mV s^{-1}	References
1	$Ti_3C_2T_x$	Symmetric	PVA/H_2SO_4	0.8	64	2	[38]
2	PANI@rGO/ $Ti_3C_2T_x$	Symmetric	1 M H_2SO_4	0.5	45.62	0.1	[39]
3	rGO/$Ti_3C_2T_x$	Asymmetric	1 M H_2SO_4	1.1	48	2	[40]
4	$Ti_3C_2T_x$	Symmetric	1 M H_2SO_4	0.8	51	1	[41]
5	$Ti_3C_2T_x$	Symmetric	6 M KOH	1	~60	5	[1]
6	$Ti_3C_2T_x$	Symmetric	1 M KOH	1	~100	2	[35]

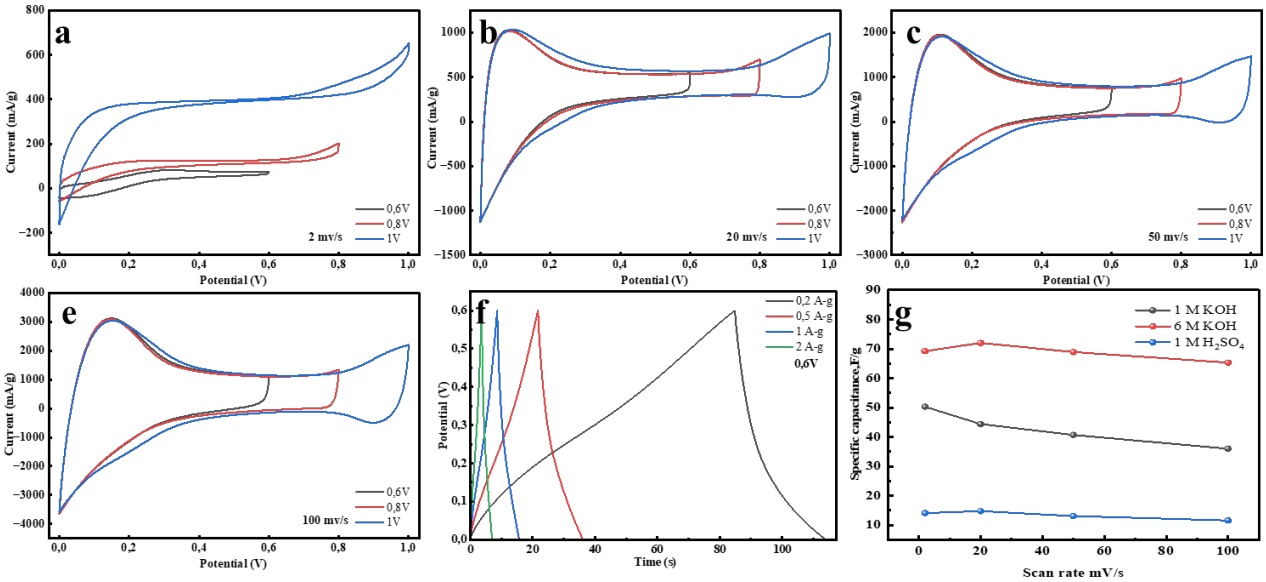

Figure 11 – Electrochemical analysis of the active material 1 M H_2SO_4 (a-f) electrolyte and specific capacitance vs scan rate for acidic, alkaline electrolytes at different scan rates (g)

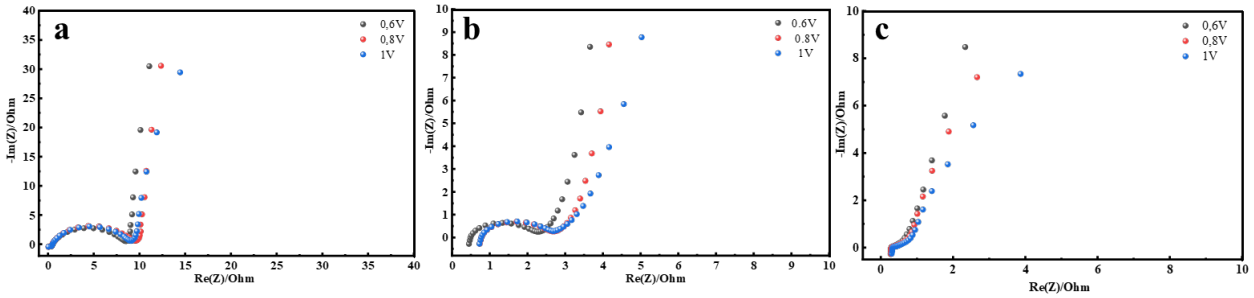

Figure 12 – EIS analysis of the active material 1 M KOH (a) and 6 M KOH (b) electrolyte and 1 M H_2SO_4 electrolyte (c) within 0.6-1.0 V

A comparison of capacitance values in different electrolytes (Figure 12g) shows a clear increasing trend in the order 1 M H_2SO_4 < 1 M KOH < 6 M KOH. The $Ti_3C_2T_x$ electrode delivers the highest capacitance in 6 M KOH, reaching ~70 F g^{-1} at 2 mV s^{-1} and ~72 F g^{-1} at 20 mV s^{-1}, indicating enhanced ionic conductivity and improved ion accessibility within the MXene layers. In contrast, the lowest capacitance is observed in 1 M H_2SO_4 (~14 F g^{-1} at 2 mV s^{-1}), reflecting slower charge-transfer kinetics and stronger polarization effects [38]. These results demonstrate that pristine multilayer $Ti_3C_2T_x$ MXene exhibits optimal capacitive behavior in concentrated alkaline electrolyte, while further performance enhancement may be achieved through composite design.

Compared to 1 M KOH, the $Ti_3C_2T_x$ MXene cell in 6 M KOH exhibits lower equivalent series resistance, as indicated by the smaller real-axis intercept in the Nyquist plots (Figure 12a,b). The reduced semicircle diameter reflects lower charge-transfer resistance, while the more vertical low-frequency region and shorter Warburg segment indicate improved capacitive behavior and faster ion diffusion in the concentrated alkaline electrolyte. In contrast, the 1 M H_2SO_4 electrolyte (Figure 12c) shows higher resistance and a more pronounced Warburg response, suggesting slower ion transport and increased polarization. These findings agree with the CV and GCD results, confirming superior electrochemical kinetics in 6 M KOH.

4. Conclusion

Multilayer $Ti_3C_2T_x$ MXene was successfully synthesized via HF etching combined with a gentle delamination approach, enabling efficient Al removal while preserving structural integrity. Structural analyses confirmed the formation of an expanded layered MXene architecture with interlayer spacing of ~1.2-1.3 nm and functionalized surfaces, accompanied by a

clear morphological transition from dense MAX-phase particles to an open accordion-like structure. Electrochemical measurements demonstrated predominantly capacitive behavior with good reversibility and rate capability in alkaline electrolytes. The electrode delivered superior capacitance in 6 M KOH, reaching ~70 F g^{-1} at 2 mV s^{-1} and ~72 F g^{-1} at 20 mV s^{-1}, while lower values of ~50 F g^{-1} were obtained in 1 M KOH and only ~14 F g^{-1} in 1 M H_2SO_4. The enhanced performance in concentrated alkaline electrolyte is attributed to improved ionic conductivity, reduced charge-transfer resistance, and accelerated ion transport within the layered MXene structure. Conversely, the acidic electrolyte exhibited stronger polarization, diffusion limitations, and reduced rate capability. Overall, this study demonstrates that electrolyte concentration and chemistry critically influence the electrochemical kinetics and charge-storage mechanism of $Ti_3C_2T_x$ MXene. The superior performance observed in concentrated alkaline electrolyte highlights the strong potential of multilayer $Ti_3C_2T_x$ MXene for aqueous supercapacitor applications, while further performance enhancement may be achieved through composite engineering.

Acknowledgements

This research was funded by the Committee of Science of the Ministry of Science and Higher Education of the Republic of Kazakhstan (Grant No. BR27198045). The authors also express their sincere gratitude to Nazarbayev University for providing facilities for physicochemical research.

CRediT Authorship Contribution Statement

A.B. Tugelbayeva: Conceptualization, Methodology, Formal analysis, Data curation, Visualization, Writing – original draft. *B.K. Balgabayeva:* Writing – review & editing. *F. Sultanov:* Formal analysis, Writing – review & editing. *Zh.A. Supiyeva:* Conceptualization, Supervision, Resources, Funding acquisition, Writing – review & editing.

Conflicts of Interest

The authors declare that they have no known competing financial interests or personal relationships that could have appeared to influence the work reported in this paper.

References

1 Koudahi MF, Frąckowiak E (2024) Small 20(21):2307165. *https://doi.org/10.1002/smll.202307165*

2 Otun KO, Mukhtar A, Hossain I, Abdulsalam J (2024) J Energy Storage 85:114127. *https://doi.org/10.1016/j.est.2024.114127*

3 Nahirniak S, Ray A, Saruhan B (2023) Batteries 9(2):126. *https://doi.org/10.3390/batteries9020126*

4 Naguib M, Kurtoglu M, Presser V, et al (2011) Adv Mater 23(37):4248–4253. *https://doi.org/10.1002/adma.201102306*

5 Anu MA, Tomy M, Manimehala U, Xavier TS (2025) Mater Res Bull 185:113315. *https://doi.org/10.1016/j.materresbull.2025.113315*

6 Naguib M, Mashtalir O, Carle J, et al (2012) ACS Nano 6(2):1322–1331. *https://doi.org/10.1021/nn204153h*

7 Otgonbayar Z, Yang S, Kim IJ, Oh WC (2023) Nanomaterials 13(5):919. *https://doi.org/10.3390/nano13050919*

8 Lepikhin MS, Ryabicheva MA, Zhigalyonok YS, et al (2025) Chem Bull Kazakh Natl Univ 115(2):32–46. *https://doi.org/10.15328/cb1382*

9 Askaruly K, Supiyeva Zh, Azat S, et al (2025) J Power Sources 659:238423. *https://doi.org/10.1016/j.jpowsour.2025.238423*

10 Sun M, Ye W, Zhang J, Zheng K (2024) Inorganics 12(4):112. *https://doi.org/10.3390/inorganics12040112*

11 Dixit P, Maiti T (2022) Ceram Int 48(24). *https://doi.org/10.1016/j.ceramint.2022.08.172*

12 Naguib M, Gogotsi Y (2015) Acc Chem Res 48(1):128–135. *https://doi.org/10.1021/ar500346b*

13 Gogotsi Y, Anasori B (2019) ACS Nano 13(8):8491–8494. *https://doi.org/10.1021/acsnano.9b06394*

14 Kumari K, Chatterjee S, Raj R, et al (2026) ACS Appl Electron Mater 8(9)4234–4246. *https://doi.org/10.1021/acsaelm.6c00378*

15 Ghidiu M, Lukatskaya MR, Zhao MQ, et al (2015) Nature 516(7529):78–81. *https://doi.org/10.1038/nature13970*

16 Maleski K, Ren CE, Zhao MQ, et al (2018) ACS Appl Mater Interfaces 10(29):24491–24498. *https://doi.org/10.1021/acsami.8b04662*

17 Zhang CJ, Pinilla S, McEvoy N, et al (2017) Chem Mater 29(11):4848–4856. *https://doi.org/10.1021/acs.chemmater.7b00745*

18 Aslam A, Nadeem N, Balgabayeva B, et al (2025) Inorg Chem Commun 181:115191. *https://doi.org/10.1016/j.inoche.2025.115191*

19 Panda S, Deshmukh K, Khadheer Pasha SK, et al (2022) Coord Chem Rev 466:214518. *https://doi.org/10.1016/j.ccr.2022.214518*

20 Arole K, Pas SE, Thakur RM, et al (2024) ACS Appl Mater Interfaces 16(46):64156–64165. *https://doi.org/10.1021/acsami.4c12659*

21 Jia XT, Xing HW, Cheng XW, et al (2025) Nanomaterials 15(3):204. *https://doi.org/10.3390/nano15030204*

22 Alonzo SMM, Bastakoti BP (2025) Mater Today Nano 32:100704. *https://doi.org/10.1016/j.mtnano.2025.100704*

23 Magesh V, Sundramoorthy AK, Ganapathy D, et al (2023) Biosensors 13(1):54. *https://doi.org/10.3390/bios13010054*

24 Adomaviciute-Grabusove S, Popov A, Ramanavicius S, et al (2024) ACS Nano 18(20):17143–17158. *https://doi.org/10.1021/acsnano.4c02150*

25 Pazniak A, Bazhin P, Shplis N, et al (2019) Mater Des 183:108143. *https://doi.org/10.1016/j.matdes.2019.108143*

26 Yao L, Tian X, Cui X, et al (2021) J Mater Sci Mater Electron 32(23):27837–27848. https://doi.org/10.1007/s10854-021-07166-w
27 Verma KD, Kar KK (2025) Chem Eng J 504:158938. https://doi.org/10.1016/j.cej.2024.158938
28 Kenzhebek M, Mentbayeva A, Supiyeva Zh, Kabyshev A, Sultanov F (2025) Mater Lett 396:138773. https://doi.org/10.1016/j.matlet.2025.138773
29 Cai Y, Chen X, Xu Y, et al (2024) Carbon Energy 6:e501. https://doi.org/10.1002/cey2.501
30 Purbayanto MAK, Jakubczak M, Bury D, et al (2022) ACS Appl Nano Mater 5(4):5067–5078. https://doi.org/10.1021/acsanm.2c00365
31 Dong Y, Wu ZS, Zheng S, et al (2017) ACS Nano 11(5):4792–4800. https://doi.org/10.1021/acsnano.7b01165
32 Liu N, Li Q, Wan H, et al (2022) Nat Commun 13(1):6249. https://doi.org/10.1038/s41467-022-33280-2
33 Anjum N, Rahman MM, Elattar A, et al (2025) Adv Sustain Syst 9(8):2500402. https://doi.org/10.1002/adsu.202500402
34 Zheng W, Halim J, Rosen J, Barsoum MW (2022) Adv Energy Sustain Res 3(2):2100147. https://doi.org/10.1002/aesr.202100147
35 Mansurov Z, Supiyeva Zh, Avchukir Kh, et al (2019) Eurasian Chem J 21(4):371–378. https://doi.org/10.18321/ectj885
36 Supiyeva Zh, Mansurov Z, Azat S, Abbas Q (2024) Front Chem 12:1377144. https://doi.org/10.3389/fchem.2024.1377144
37 Feng S, Wang X, Wang M, et al (2021) Nano Lett 21(18)7561–7568. https://doi.org/10.1021/acs.nanolett.1c02071
38 Liu Y, Zhou H, Zhou W, Meng S, Qi C, Liu Z, Kong T (2021) Adv Energy Mater 11(30):2101329. https://doi.org/10.1002/aenm.202101329
39 Navarro-Suárez AM, Van Aken KL, Mathis T, et al (2018) Electrochim Acta 259:752–765. https://doi.org/10.1016/j.electacta.2017.10.125
40 Rakhi RB, Ahmed B, Hedhili MN, Anjum DH, Alshareef HN (2015) Chem Mater 27(15):5314–5323. https://doi.org/10.1021/acs.chemmater.5b01623
41 Murugesan RA, Nagamuthu Raja KC (2023) Mater Res Bull 163:112217. https://doi.org/10.1016/j.materresbull.2023.112217

Information about the authors:

A.B. Tugelbayeva – Researcher, Satbayev University (Almaty, Kazakhstan, e-mail: aigul.tugelbaeva00@gmail.com);

B.K. Balgabayeva – Master student / Junior Researcher, Satbayev University; al-Farabi Kazakh National University, (Almaty, Kazakhstan, e-mail: balaussa.balgabayeva002@gmail.com);

F. Sultanov – PhD, Professor, National Laboratory Astana, Nazarbayev University (Astana, Kazakhstan, e-mail: fail.sultanov@nu.edu.kz);

Zh.A. Supiyeva – PhD, Associate Professor, Satbayev University; al-Farabi Kazakh National University (Almaty, Kazakhstan, e-mail: zhazira.supiyeva@kaznu.kz).